

An optical transmission spectrum of the giant planet WASP-36 b

L. Mancini^{1,2*}, J. Kemmer¹, J. Southworth³, K. Bott⁴, P. Mollière¹, S. Ciceri¹, G. Chen⁵, Th. Henning¹

¹Max Planck Institute for Astronomy, Königstuhl 17, 69117 – Heidelberg, Germany

²INAF – Osservatorio Astrofisico di Torino, via Osservatorio 20, 10025 – Pino Torinese, Italy

³Astrophysics Group, Keele University, Keele ST5 5BG, UK

⁴Exoplanetary Science at UNSW, Australian Centre for Astrobiology, School of Physics, UNSW Australia

⁵Key Laboratory of Planetary Sciences, Purple Mountain Observatory, Chinese Academy of Sciences, Nanjing 210008, China

Accepted XXX. Received YYY; in original form ZZZ

ABSTRACT

We present broad-band photometry of five transits in the planetary system WASP-36, totaling 17 high-precision light curves. Four of the transits were simultaneously observed in four passbands (g' , r' , i' , z'), using the telescope-defocussing technique, and achieving scatters of less than 1 mmag per observation. We used these data to improve the measured orbital and physical properties of the system, and obtain an optical transmission spectrum of the planet. We measured a decreasing radius from bluer to redder passbands with a confidence level of more than 5σ . The radius variation is roughly 11 pressure scale heights between the g' and the z' bands. This is too strong to be Rayleigh scattering in the planetary atmosphere, and implies the presence of a species which absorbs strongly at bluer wavelengths.

Key words: stars: planetary systems – stars: fundamental parameters – stars: individual: WASP-36 – techniques: photometric

1 INTRODUCTION

Transiting hot Jupiters are a class of exoplanets which are very suitable for detailed study of their physical and orbital parameters. They are gas-giant planets with short orbital periods (mass $M_p > 0.3M_{\text{Jup}}$ and period $P < 10$ d), and many of them are now known orbiting bright stars. Their relatively large sizes usually give deep transits (typically 0.5–3.5%) which are well-suited for observation and analysis. Another particular advantage of transiting hot Jupiters is their suitability for *transmission spectroscopy*, which can yield constraints on the chemical composition at the terminator of their atmospheres from transit depth measurements at multiple wavelengths. Depending on the temperature of the planet’s atmosphere, it is possible to investigate the presence of several molecules (e.g. H₂O, CO, CO₂ and CH₄) at infrared (IR) wavelengths. The blue region of the visual wavelength range is also important to study, as it allows constraints to be placed on the presence of Rayleigh scattering or particular atomic absorption features (e.g. Na). There has been significant progress in this field in the last

few years, and many exoplanets have been observed using transmission spectroscopy. The resulting transmission spectra show an unexpectedly diversity of the atmospheres of hot Jupiters, in particular the amount of cloud at observable pressure levels (Sing et al. 2016).

Whilst most of these studies were performed at IR wavelengths, a small set of planets have also been studied at optical wavelengths from space with the Hubble and the Spitzer telescopes (i.e. HD 189733 b: Pont et al. 2013; HD 209458 b: Désert et al. 2008; HAT-P-1 b: Nikolov et al. 2014; HAT-P-12 b: Sing et al. 2016; WASP-6 b: Nikolov et al. 2015; WASP-12 b: Sing et al. 2013; WASP-17 b: Sing et al. 2016; WASP-19 b: Huitson et al. 2013; WASP-31 b: Sing et al. 2015; WASP-39 b: Fischer et al. 2016;) and from large ground-based telescopes such as the Very Large Telescope (GJ 1214 b: Bean et al. 2010, 2011; WASP-19 b: Sedaghati et al. 2015), the Gran Telescopio CANARIAS (HAT-P-19 b: Mallonn et al. 2015; WASP-43 b: Murgas et al. 2014), Gemini (HAT-P-32: Gibson et al. 2013a; WASP-12: Stevenson et al. 2014; WASP-29: Gibson et al. 2013b) and Magellan (HAT-P-26: Stevenson et al. 2015; TrES-3: Parviainen et al. 2016; WASP-6: Jordàn et al. 2013).

* E-mail: mancini@mpia.de

An alternative approach for probing planetary atmospheres is that of *transmission photometry*, which has a lower spectral resolution but is suitable for ground-based telescopes with smaller apertures and exoplanets orbiting faint stars. Moreover, photometric observations are much less affected by telluric contamination than spectroscopic ones.

In this context, we are carrying out a large program of transit observations of the known hot Jupiters with an array of medium-size telescopes in both hemispheres (Mancini & Southworth 2016). In particular, we are using GROND (Gamma-Ray Burst Optical and Near-Infrared Detector), an imaging camera able to obtain light curves in four optical and three near-IR passbands simultaneously. These are used to improve measurements of the physical properties of the planets and their host stars, and to look for transit-depth variations as a function of wavelength in the optical wavelength region.

In order to have a comprehensive picture, we are investigating both inflated and compact hot Jupiters. Due to their density, the latter should be not optimal targets for transmission-spectrum studies. However, depending on the equilibrium temperature, opacity and chemical composition of their atmospheres, Mie scattering, Rayleigh scattering and molecular opacity could still cause strong variation of the radius of such planets, especially if we compare measurements at the wavelength region 400 – 500 nm with those at 800 – 900 nm.

Previous studies with GROND have shown different atmospheric properties: we obtained transmission photometry consistent with flat spectra for several systems (WASP-23 b: Nikolov et al. 2013; WASP-43 b: Chen et al. 2014; WASP-80 b: Mancini et al. 2014a; WASP-67 b: Mancini et al. 2014b), and larger planetary radii at bluer wavelengths for two objects (Qatar-2 b: Mancini et al. 2014c; WASP-103: Southworth et al. 2015). These two latter studies were based on multiple transit observations from GROND and demonstrate that repeated transit observations produce more precise and robust results. It is interesting to note the large variation that was found in the dense and moderately cold planet Qatar-2 b.

In the present work, we study the transiting planetary system WASP-36 (Smith et al. 2012). This contains a relatively dense hot Jupiter, WASP-36 b, with mass $M_p \approx 2.3 M_{\text{Jup}}$ and radius $R_p \approx 1.3 R_{\text{Jup}}$. The density of WASP-36 b is therefore similar to that of Qatar-2 b, but its temperature is higher since it orbits a hotter (5959 ± 134 K) and metal-poor ($[\text{Fe}/\text{H}] = -0.26 \pm 0.10$) G2 V star, WASP-36 A, every 1.54 days. The high temperature and low densities imply that the planet atmosphere would be rich of molecules consisting of hydrogen and sulfur, which are able to absorb stellar light at blue-optical wavelengths.

An occultation event of WASP-36 b was observed in the K_s band by Zhou et al. (2015). These authors found that the orbit is consistent with circular and that the occultation is $0.13 \pm 0.04\%$ deep, corresponding to a K_s -band brightness temperature of $T_B = 1900_{-200}^{+100}$ K. This is similar to the planet's equilibrium temperature ($T'_{\text{eq}} \approx 1725$ K) and means that strong absorbers are expected to be present in its atmosphere (Fortney et al. 2010). Maciejewski et al. (2016) has recently presented a new photometric light curve of a WASP-36 b transit, which was used to redetermine the parameters of the planetary system.

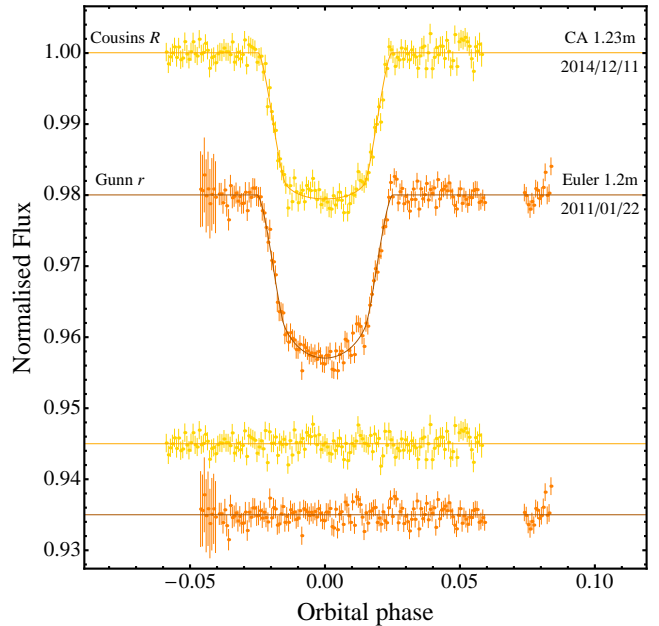


Figure 1. Transit light curve from Calar Alto (upper; this work) and the best one from the discovery paper (lower; Smith et al. 2012). The dates and filters used are indicated. The solid lines show the JKTEBOP best fits and the residuals are shown at the bottom.

The paper is structured as follows. The observations and data reduction are both described in Sect. 2, while the analysis of the data is presented in Sect. 3. The refinement of the orbital ephemerides is given in Sect. 3. In Sect. 4 we revise the main physical properties of the planetary system. In Sect. 5 we investigate the variation of the planetary radius as function of wavelength and, finally, we summarize our results in Sect. 6.

2 OBSERVATION AND DATA REDUCTION

Four transits by WASP-36 b were observed with GROND, which is mounted on the MPG 2.2 m telescope at ESO La Silla (Table 1). GROND is a seven-channel imaging camera that was built for rapid observations of gamma-ray burst afterglows (Greiner et al. 2008), but is also well-suited for transit observations. GROND can be used to observe simultaneously in four optical passbands (similar to Sloan g', r', i', z') and three near-IR bands (J, H, K). The optical light is collected by back-illuminated 2048×2048 pixel E2V CCDs, with a field of view of $5.4 \text{ arcmin} \times 5.4 \text{ arcmin}$ at a scale of $0.158 \text{ arcsec pixel}^{-1}$. The near-IR channels use 1024×1024 pixel Rockwell HAWAII-1 arrays, with a field of view of $10 \text{ arcmin} \times 10 \text{ arcmin}$ at $0.6 \text{ arcsec pixel}^{-1}$. The photometric precision of the near-IR arms is significantly worse than the optical ones (Pierini et al. 2012), so these data will be not considered in this work.

Another transit by WASP-36 b was remotely observed in December 2014 through a Cousins R filter with the Zeiss 1.23 m telescope at the Calar Alto Observatory. The telescope is equipped with a 4096×4096 pixel DLR-MKIII camera, with a field of view of $21.5 \text{ arcmin} \times 21.5 \text{ arcmin}$ at a plate scale of $0.32 \text{ arcsec pixel}^{-1}$. The CCD was oper-

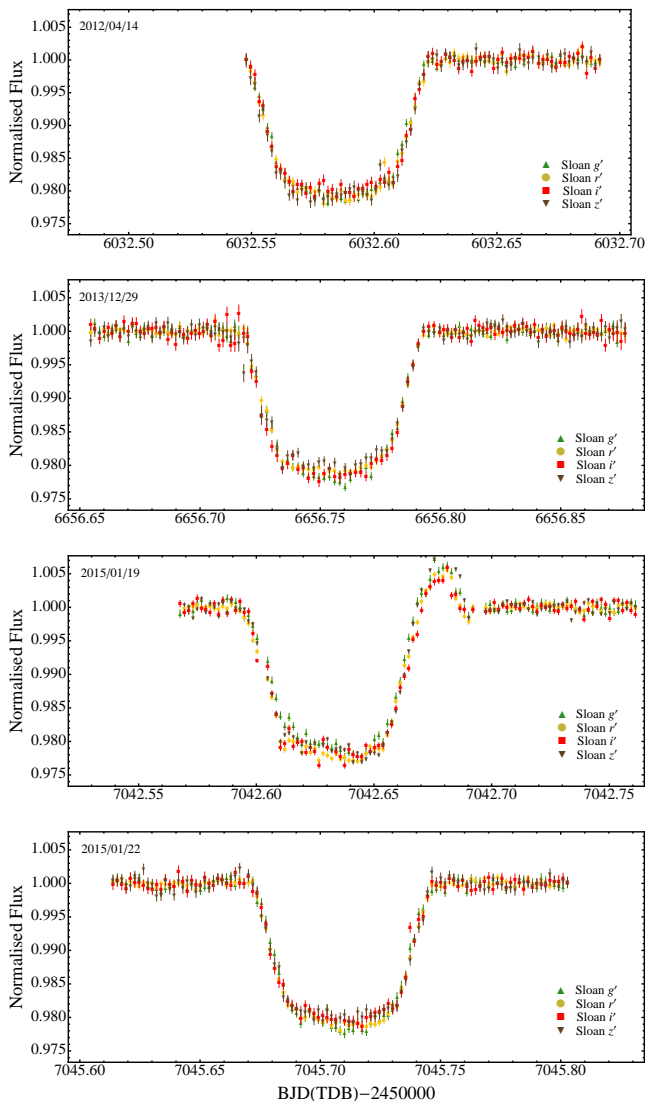


Figure 2. The four transit light curves from GROND, ordered according to date.

ated without binning, but windowed to shorten the readout time. During all the observations the two telescopes were autoguided and defocused in order to improve the photometric precision of the data.

The reduction of the data was performed using the DEFOT pipeline, written in IDL¹ (Southworth et al. 2014). Briefly, the scientific images were calibrated using master bias and flat-field frames, produced by median-combining individual calibration images. The target and a suitable set of non-variable comparison stars were identified in a reference image, which was used to measure pointing variations by a cross-correlation process. Three apertures were placed by hand around the selected stars and the aperture radii were chosen to obtain the lowest scatter versus a fitted model. Differential photometry was obtained using the APER routine²

¹ The acronym IDL stands for Interactive Data Language and is a trademark of ITT Visual Information Solutions.

² APER is part of the ASTROLIB subroutine library distributed by NASA.

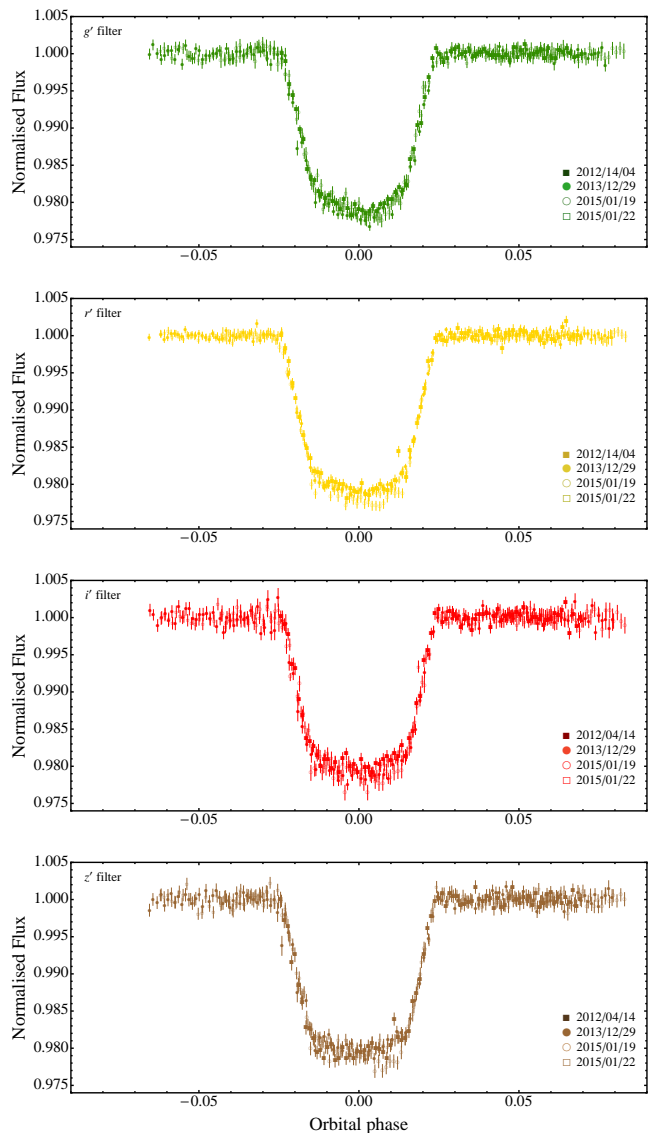


Figure 3. As Fig. 2 but sorted according to filter.

and rectified to zero magnitude by fitting a straight line to the out-of-transit data. The data will be made available at the CDS³.

The Calar Alto light curve is plotted in Fig. 1 together with the best one reported in the discovery paper (Smith et al. 2012) for comparison. The GROND light curves are plotted according to date in Fig. 2 and to filter in Fig. 3. A clear anomaly is visible in the GROND data observed on January 19, 2015 (third panel in Fig. 2). This variation is not correlated with the position of the stars on the CCDs, the CCD temperatures, the weather conditions, or vignetting from the dome slit. There is also no obvious astrophysical explanation. We therefore assumed that the anomaly was caused by an unknown instrumental effect and removed the affected data from our analysis.

³ <http://cdsweb.u-strasbg.fr/>

Table 1. Details of the transit observations presented in this work. N_{obs} is the number of observations, T_{exp} is the exposure time, T_{obs} is the observational cadence, and ‘Moon illum.’ is the geocentric fractional illumination of the Moon at midnight (UT). The aperture sizes are the radii of the software apertures for the star, inner sky and outer sky, respectively. Scatter is the *rms* scatter of the data versus a fitted model.

Telescope	Date of first obs	Start time (UT)	End time (UT)	N_{obs}	T_{exp} (s)	T_{obs} (s)	Filter	Airmass	Moon illum.	Aperture radii (px)	Scatter (mmag)
MPG 2.2 m	2012 04 15	01:44	04:36	82	90	156	Sloan g'	1.12 → 2.70	23%	30,53,90	0.54
MPG 2.2 m	2012 04 15	01:44	04:36	82	90	156	Sloan r'	1.12 → 2.70	23%	32,68,85	0.69
MPG 2.2 m	2012 04 15	01:44	04:36	82	90	156	Sloan i'	1.12 → 2.70	23%	25,55,80	0.76
MPG 2.2 m	2012 04 15	01:44	04:36	82	90	156	Sloan z'	1.12 → 2.70	23%	30,58,90	0.84
MPG 2.2 m	2013 12 30	03:42	08:57	121	100	142	Sloan g'	1.85 → 1.07 → 1.23	2%	27,65,90	0.69
MPG 2.2 m	2013 12 30	03:42	08:57	122	100	142	Sloan r'	1.85 → 1.07 → 1.23	2%	27,65,90	0.44
MPG 2.2 m	2013 12 30	03:42	08:57	124	100	142	Sloan i'	1.85 → 1.07 → 1.23	2%	19,61,90	0.88
MPG 2.2 m	2013 12 30	03:42	08:57	121	100	142	Sloan z'	1.85 → 1.07 → 1.23	2%	32,63,91	0.87
CA 1.23 m	2014 12 11	01:44	06:02	154	90	100	Cousins R	1.66 → 1.42 → 1.79	80%	23,33,60	1.21
MPG 2.2 m	2015 01 20	01:37	06:16	88	110	156	Sloan g'	2.04 → 1.07 → 1.08	0%	26,66,100	0.83
MPG 2.2 m	2015 01 20	01:37	06:16	88	110	156	Sloan r'	2.04 → 1.07 → 1.08	0%	24,62,100	0.61
MPG 2.2 m	2015 01 20	01:37	06:16	87	110	156	Sloan i'	2.04 → 1.07 → 1.08	0%	24,60,90	0.95
MPG 2.2 m	2015 01 20	01:37	06:16	87	110	156	Sloan z'	2.04 → 1.07 → 1.08	0%	29,66,100	0.83
MPG 2.2 m	2015 01 23	02:43	07:16	105	110	156	Sloan g'	1.39 → 1.07 → 1.19	10%	34,94,110	0.65
MPG 2.2 m	2015 01 23	02:43	07:16	101	110	156	Sloan r'	1.39 → 1.07 → 1.19	10%	29,55,97	0.43
MPG 2.2 m	2015 01 23	02:43	07:16	104	110	156	Sloan i'	1.39 → 1.07 → 1.19	10%	30,53,88	0.76
MPG 2.2 m	2015 01 23	02:43	07:16	103	110	156	Sloan z'	1.39 → 1.07 → 1.19	10%	31,59,107	0.75

3 LIGHT CURVE ANALYSIS

We have modelled our new light curves and the best one from [Smith et al. \(2012\)](#), which was observed with the Euler 1.2 m telescope, using the JKTEBOP⁴ code ([Southworth 2013](#)). Each light curve was fitted using the following parameters: the sum and ratio of the fractional radii⁵ ($r_A + r_b$ and $k = r_b/r_A$), the orbital period and inclination (P and i), the time of transit midpoint (T_0) and the linear coefficient of the quadratic limb darkening law (u_A). The second limb darkening coefficient (v_A) was fixed to a theoretical value ([Claret et al. 2004](#)). We assumed that the orbit of WASP-36 b is circular ([Smith et al. 2012](#); [Zhou et al. 2015](#)).

The APER algorithm, used in our reduction pipeline, usually underestimates the uncertainties in the differential magnitudes. Red noise also affects time-series photometry as it is not accounted for by standard error estimation algorithms (e.g. [Carter & Winn 2009](#)). We therefore rescaled the error bars to give a reduced χ^2 of $\chi^2_\nu = 1$ (e.g. [Mancini et al. 2014a](#); [Southworth et al. 2015](#)). Moreover, using the likelihood function defined as in Eq. (32) of [Carter & Winn \(2009\)](#), we performed a wavelet-basis red-noise MCMC analysis for estimating the Gaussian white noise and the correlated red noise for each light curve. They are reported in the last two columns of Table 3. Fig. 5 shows the root mean square of the binned residuals versus the bin size, which is another way to illustrate the photometric precision that we achieved.

⁴ JKTEBOP is written in FORTRAN77 and is available at: <http://www.astro.keele.ac.uk/jkt/codes/jktebop.html>

⁵ The fractional radii are defined as $r_A = R_A/a$ and $r_b = R_b/a$, where R_A and R_b are the true radii of the star and planet, and a is the semi-major axis.

3.1 Orbital period determination

We estimated the times of mid-transit by fitting each light curve with JKTEBOP. The uncertainties were obtained using Monte Carlo simulations. We also considered the timing measured by [Smith et al. \(2012\)](#) and [Maciejewski et al. \(2016\)](#). All transit timings (see Table 2) were then fitted with a straight line to obtain the following orbital ephemeris:

$$T_0 = \text{BJD(TDB)} 2455569.83771(46) + 1.53736596(24) E,$$

where E denotes the number of orbital cycles after the reference epoch, and the quantities in brackets denote the uncertainty in the final digit of the preceding number. The residuals of the fit are plotted in Fig. 6. The linear ephemeris is not a good match to the observations – the fit has $\chi^2_\nu = 3.76$ – so the uncertainties have been increased to account for this. As our timings comprise only ten epochs over more than 1000 orbits, and in line with previous work (e.g. [Southworth et al. 2014](#); [Ciceri et al. 2015](#); [Mancini et al. 2015](#)), we do not interpret this as an indication of transit time variations.

3.2 Photometric parameters

The best fits to the light curves are shown in Fig. 1 and Fig. 4. The parameters of the fits are reported in Table 3. The uncertainties of the parameters were estimated for each solution from 10 000 Monte Carlo simulations and through a residual-permutation algorithm. The larger of the two error bars was adopted in each case. The final photometric parameters were calculated as the weighted mean of the results in Table 3. We also show the values obtained by [Smith et al. \(2012\)](#) and [Maciejewski et al. \(2016\)](#) for comparison.

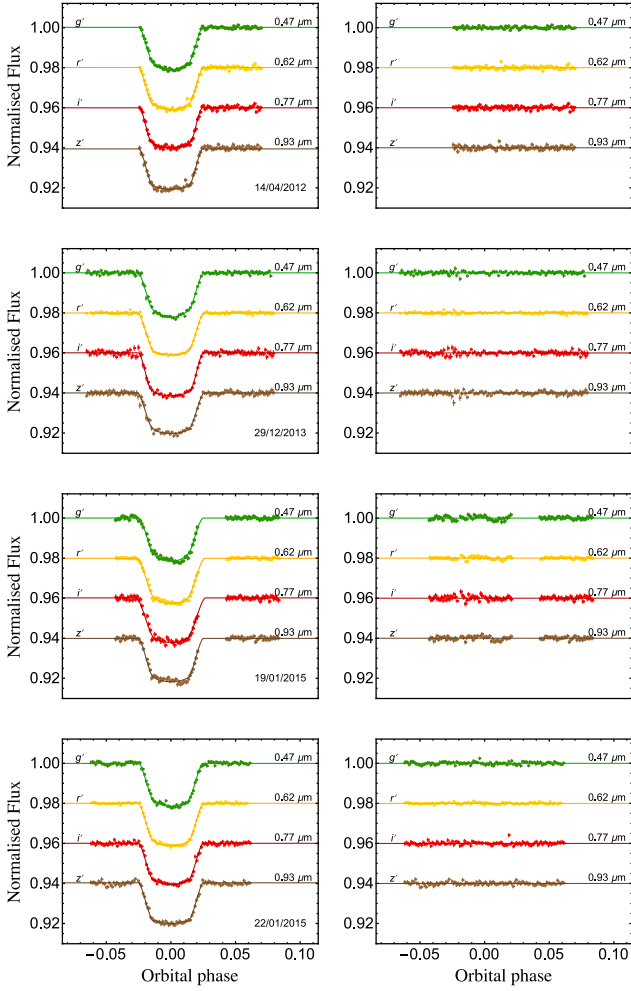


Figure 4. Phased light curves of WASP-36 from GROND compared to the JKTEBOP best fits. The passbands and central wavelengths are labelled.

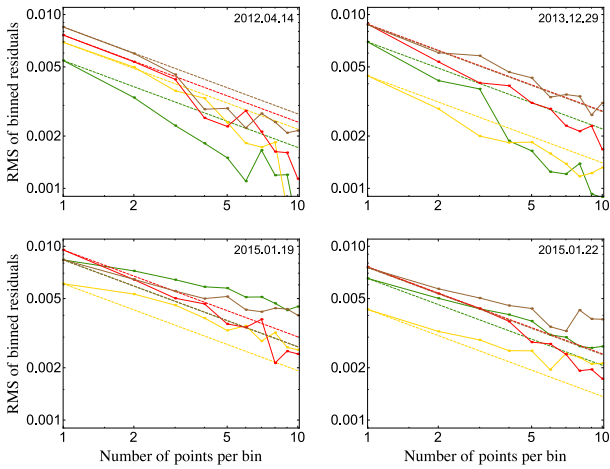


Figure 5. Root mean square of binned residuals versus the number of points per bin for each of the four transits of WASP-36 observed with GROND and for each filter: green line is g' , yellow line is r' , red line is i' and brown line is z' . The dashed lines are proportional to $N^{-1/2}$ and are normalized to match the value for bin size $N = 1$ for each light curve.

Table 2. Times of transit midpoint of WASP-36 and their residuals.

Time of minimum BJD(TDB)–2400000	Cycle no.	O-C (JD)	Reference
5556.00221 ± 0.00055	-9	0.00075091	Smith et al. (2012)
5563.68781 ± 0.00017	-4	-0.00047861	Smith et al. (2012)
5577.52413 ± 0.00025	5	-0.00045174	Smith et al. (2012)
5583.67336 ± 0.00021	9	-0.00068535	Smith et al. (2012)
6003.37465 ± 0.00043	282	0.00013033	Maciejewski et al. (2016)
6032.58490 ± 0.00028	301	0.00001463	g' MPG 2.2 m
6032.58515 ± 0.00031	301	0.00025994	r' MPG 2.2 m
6032.58545 ± 0.00025	301	0.00055714	i' MPG 2.2 m
6032.58551 ± 0.00031	301	0.00062418	z' MPG 2.2 m
6656.75514 ± 0.00024	707	-0.00030923	g' MPG 2.2 m
6656.75532 ± 0.00012	707	-0.00012608	r' MPG 2.2 m
6656.75493 ± 0.00014	707	-0.00051748	i' MPG 2.2 m
6656.75517 ± 0.00030	707	-0.00027314	z' MPG 2.2 m
7002.66248 ± 0.00012	932	-0.00029382	CA 1.23 m
7042.63387 ± 0.00033	958	-0.00041580	g' MPG 2.2 m
7042.63299 ± 0.00024	958	-0.00130137	r' MPG 2.2 m
7042.63336 ± 0.00044	958	-0.00093176	i' MPG 2.2 m
7042.63352 ± 0.00022	958	-0.00076909	z' MPG 2.2 m
7045.70910 ± 0.00015	960	0.00008466	g' MPG 2.2 m
7045.70899 ± 0.00010	960	-0.00002979	r' MPG 2.2 m
7045.70878 ± 0.00035	960	-0.00023732	i' MPG 2.2 m
7045.70915 ± 0.00018	960	0.00013033	z' MPG 2.2 m

4 PHYSICAL PROPERTIES

We have determined the physical properties of the system using the *Homogeneous Studies* approach (Southworth 2012). The input quantities to this analysis were the photometric parameters (Sect. 3.2) and the spectroscopic properties of the host star taken from Smith et al. (2012) (effective temperature $T_{\text{eff}} = 5959 \pm 134$ K, metallicity $[\frac{\text{Fe}}{\text{H}}] = -0.26 \pm 0.10$ and velocity amplitude $K_A = 391.5 \pm 8.3$ m s^{-1}). These were augmented by an estimate of the velocity amplitude of the planet, K_b , and the physical properties of the system calculated.

K_b was iteratively adjusted to maximise the agreement between the measured R_A/a and T_{eff} and those predicted by a set of theoretical models, considering a wide range of possible ages for the host star. Five sets of theoretical models were used (Claret: Claret et al. 2004; Y2: Demarque et al. 2004; BaSTI: Pietrinferni et al. 2004; VRSS: VandenBerg et al. 2006; DSEP: Dotter et al. 2008), yielding five different estimates of each output quantity. We took the unweighted mean of these as the final values, and assigned a systematic error based on the level of agreement among the values obtained using different theoretical models. Statistical errors were propagated through the analysis from the input parameters. The final values are given in Table 4. Our results are in good agreement with those found by Smith et al. (2012) and Maciejewski et al. (2016), but are more precise and robust.

5 VARIATION OF THE PLANETARY RADIUS WITH WAVELENGTH

Being strongly irradiated by their parent stars, the spectra of hot Jupiters are expected to show characteristic absorp-

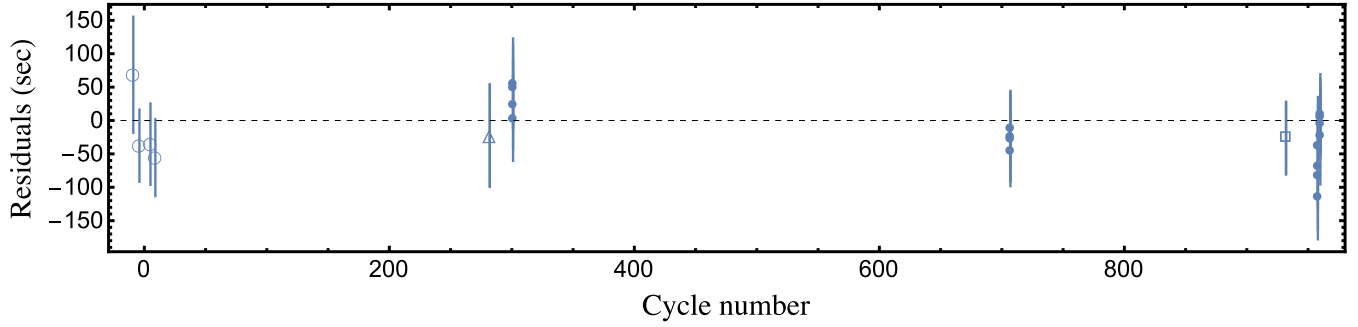


Figure 6. Residuals of the times of mid-transit versus a linear ephemeris. The timings from [Smith et al. \(2012\)](#) are plotted using open circles, from [Maciejewski et al. \(2016\)](#) with a triangle, from GROND with filled circles, and from Calar Alto with an open box.

Table 3. Photometric properties of the WASP-36 system derived by fitting the light curves. σ_{white} is the Gaussian white noise, while σ_{red} indicates the correlated red noise, which is defined in [Carter & Winn \(2009\)](#).

Source	Filter	$r_A + r_b$	k	i°	r_A	r_b	$\sigma_{\text{red}} (10^{-3})$	$\sigma_{\text{white}} (10^{-3})$
MPG 2.2 m/GROND #1	Sloan g'	0.1908 ± 0.0047	0.1411 ± 0.0051	83.34 ± 0.34	0.1672 ± 0.0041	0.02359 ± 0.00091	$0.97^{+1.07}_{-0.66}$	$0.41^{+0.05}_{-0.06}$
MPG 2.2 m/GROND #1	Sloan r'	0.1917 ± 0.0087	0.1387 ± 0.0077	83.47 ± 0.66	0.1683 ± 0.0076	0.0233 ± 0.0015	$1.17^{+1.20}_{-0.79}$	$0.57^{+0.07}_{-0.07}$
MPG 2.2 m/GROND #1	Sloan i'	0.178 ± 0.012	0.128 ± 0.010	84.64 ± 0.95	0.158 ± 0.011	0.0203 ± 0.0017	$1.86^{+1.48}_{-1.19}$	$0.49^{+0.07}_{-0.11}$
MPG 2.2 m/GROND #1	Sloan z'	0.189 ± 0.012	0.135 ± 0.014	83.50 ± 0.77	0.167 ± 0.012	0.0225 ± 0.0015	$1.58^{+1.30}_{-1.00}$	$0.63^{+0.08}_{-0.08}$
MPG 2.2 m/GROND #2	Sloan g'	0.194 ± 0.010	0.1363 ± 0.0033	83.62 ± 0.89	0.1704 ± 0.0084	0.0232 ± 0.0017	$1.15^{+1.11}_{-0.79}$	$0.64^{+0.07}_{-0.06}$
MPG 2.2 m/GROND #2	Sloan r'	0.204 ± 0.013	0.136 ± 0.010	82.56 ± 0.49	0.180 ± 0.013	0.02459 ± 0.00085	$1.90^{+1.41}_{-1.22}$	$0.81^{+0.09}_{-0.09}$
MPG 2.2 m/GROND #2	Sloan i'	0.1845 ± 0.0063	0.1347 ± 0.0017	84.33 ± 0.56	0.1626 ± 0.0053	0.02190 ± 0.00093	$1.19^{+0.93}_{-0.75}$	$0.40^{+0.05}_{-0.06}$
MPG 2.2 m/GROND #2	Sloan z'	0.2031 ± 0.0078	0.1334 ± 0.0014	82.77 ± 0.56	0.1792 ± 0.0067	0.0239 ± 0.0011	$2.97^{+1.62}_{-1.45}$	$0.73^{+0.11}_{-0.12}$
MPG 2.2 m/GROND #3	Sloan g'	0.194 ± 0.019	0.1361 ± 0.0038	83.29 ± 1.22	0.171 ± 0.016	0.0233 ± 0.0028	$4.59^{+0.67}_{-0.83}$	$0.22^{+0.16}_{-0.15}$
MPG 2.2 m/GROND #3	Sloan r'	0.2076 ± 0.0057	0.1410 ± 0.0014	82.52 ± 0.40	0.1819 ± 0.0048	0.02567 ± 0.00084	$1.34^{+1.33}_{-0.92}$	$0.72^{+0.08}_{-0.07}$
MPG 2.2 m/GROND #3	Sloan i'	0.214 ± 0.014	0.1406 ± 0.0021	82.13 ± 0.88	0.188 ± 0.012	0.0264 ± 0.0020	$3.45^{+0.46}_{-0.53}$	$0.14^{+0.12}_{-0.09}$
MPG 2.2 m/GROND #3	Sloan z'	0.1958 ± 0.0084	0.1376 ± 0.0016	83.19 ± 0.61	0.1721 ± 0.0072	0.0237 ± 0.0012	$3.59^{+1.24}_{-1.10}$	$0.45^{+0.11}_{-0.14}$
MPG 2.2 m/GROND #4	Sloan g'	0.1958 ± 0.0057	0.144 ± 0.011	82.88 ± 0.33	0.1711 ± 0.0059	0.0247 ± 0.0012	$3.15^{+1.28}_{-1.12}$	$0.42^{+0.10}_{-0.15}$
MPG 2.2 m/GROND #4	Sloan r'	0.1962 ± 0.0061	0.1357 ± 0.0074	83.21 ± 0.42	0.1727 ± 0.0062	0.02344 ± 0.00083	$3.09^{+1.80}_{-1.60}$	$0.54^{+0.11}_{-0.18}$
MPG 2.2 m/GROND #4	Sloan i'	0.194 ± 0.011	0.138 ± 0.011	83.21 ± 0.71	0.1704 ± 0.0097	0.0234 ± 0.0015	$2.00^{+0.80}_{-0.66}$	$0.27^{+0.06}_{-0.09}$
MPG 2.2 m/GROND #4	Sloan z'	0.1955 ± 0.0078	0.1414 ± 0.0089	83.02 ± 0.47	0.1713 ± 0.0076	0.0242 ± 0.0012	$3.61^{+1.26}_{-1.15}$	$0.46^{+0.11}_{-0.15}$
CA 1.23 m	Cousins R	0.192 ± 0.0073	0.1344 ± 0.0012	83.41 ± 0.62	0.1692 ± 0.0062	0.02275 ± 0.00099	$4.27^{+1.80}_{-1.91}$	$0.80^{+0.09}_{-0.10}$
Euler 1.2 m	Gunn r	0.1902 ± 0.0072	0.1397 ± 0.0022	83.77 ± 0.63	0.1669 ± 0.0060	0.023 ± 0.0012	$2.23^{+1.79}_{-1.47}$	$0.86^{+0.07}_{-0.07}$
Final results		0.1947 ± 0.0018	0.13677 ± 0.00056	83.15 ± 0.13	0.1710 ± 0.0016	0.02369 ± 0.00027		
Smith et al. (2012)		–	0.13842 ± 0.00072	83.61 ± 0.21	–	–		
Maciejewski et al. (2016)		–	$0.1391^{+0.0011}_{-0.0012}$	$83.62^{+0.30}_{-0.26}$	–	–		

tion features at optical wavelengths. Some of the predicted features include sodium (~ 590 nm), potassium (~ 770 nm), water vapour (~ 950 nm), and Rayleigh scattering at bluer wavelengths. However, the variety of hot-Jupiter transmission spectra suggests a great deal of variation in chemistry and atmospheric dynamics. While [Fortney et al. \(2005\)](#) suggested that a physical dichotomy exists between, essentially, insulated and non-insulated and well-mixed atmospheres (based primarily upon the level of irradiation received by the planet) the species of clouds driving the insulation has been disputed (e.g. [Fortney et al. 2008](#); [Zahnle et al. 2009](#); [Knutson et al. 2010](#)).

The ability of GROND to observe simultaneously in four optical bands makes it a useful tool to detect absorption features and thus probe the atmospheric composition of the planet, by measuring the ratio of the radii in different bands and comparing these values with synthetic spectra. Follow-

ing the approach of [Southworth et al. \(2015\)](#), we calculated the ratio of the radii in each passband with the other photometric parameters fixed to the best-fit values. This yielded a set of k values which are directly comparable and whose errorbars exclude common sources of uncertainty. The errorbars were calculated using 10 000 Monte Carlo simulations. We found $k_{g'} = 0.13789 \pm 0.00032$, $k_{r'} = 0.13720 \pm 0.00027$, $k_{i'} = 0.13566 \pm 0.00033$ and $k_{z'} = 0.13439 \pm 0.00035$ (Fig. 7).

A significant variation of the planetary radius was found between the g' and the z' bands. The variation is roughly 11 pressure scale heights⁶ and is significant at beyond the 5σ level. A similar variation has been found in other cases (e.g. HD 189733 b, [Sing et al. 2011](#); HAT-P-5 b,

⁶ The pressure scale height is defined as $H = \frac{k_B T_{\text{eq}}'}{\mu_m g_p}$, where k_B is Boltzmann's constant and μ_m the mean molecular weight.

Table 4. Physical parameters of the planetary system WASP-36 derived in this work and compared with results from the literature. Where two errorbars are given, the first refers to the statistical uncertainties and the second to the systematic errors.

Quantity	Symbol	Unit	This work	Smith et al. (2012)	Maciejewski et al. (2016)
Stellar mass	M_A	M_\odot	$1.081 \pm 0.025 \pm 0.023$	1.040 ± 0.031	–
Stellar radius	R_A	R_\odot	$0.985 \pm 0.012 \pm 0.007$	0.951 ± 0.018	$0.960^{+0.020}_{-0.019}$
Stellar surface gravity	$\log g_A$	cgs	$4.486 \pm 0.009 \pm 0.003$	4.499 ± 0.012	$4.490^{+0.026}_{-0.024}$
Stellar density	ρ_A	ρ_\odot	1.132 ± 0.032	1.211 ± 0.050	$1.176^{+0.060}_{-0.066}$
Planetary mass	M_b	M_{Jup}	$2.361 \pm 0.062 \pm 0.033$	2.303 ± 0.068	2.295 ± 0.058
Planetary radius	R_b	R_{Jup}	$1.327 \pm 0.019 \pm 0.009$	1.281 ± 0.029	$1.330^{+0.030}_{-0.029}$
Planetary surface gravity	g_b	m s^{-2}	33.2 ± 1.1	32.1 ± 1.3	$33.7^{+1.5}_{-1.4}$
Planetary density	ρ_b	ρ_{Jup}	$0.945 \pm 0.041 \pm 0.007$	1.096 ± 0.067	$0.976^{+0.070}_{-0.068}$
Equilibrium temperature	T'_{eq}	K	1733 ± 19	1724 ± 43	–
Safronov number	Θ		$0.0880 \pm 0.0023 \pm 0.0006$	–	–
Orbital semi-major axis	a	au	$0.02677 \pm 0.00021 \pm 0.00019$	0.02643 ± 0.00026	0.02641 ± 0.00026
Age	τ	Gyr	$1.4^{+0.4+1.4}_{-0.3-3.4}$	$2.5^{+3.5}_{-2.2}$	–

Southworth et al. 2012; GJ 3470 b, Nascimbeni et al. 2013; Qatar-2 b, Mancini et al. 2014c) and could be a sign of Rayleigh-scattering processes in the planetary atmosphere.

We also considered the possibility that unocculted starspots, which have a stronger effect at bluer wavelengths, can cause a larger radius of WASP-36 b in the blue band than that predicted by theoretical models. We estimated the effect of unocculted starspots on the transmission spectrum of WASP-36 b using the methodology described by Sing et al. (2011). The correction to the transit depth for unocculted spots is plotted in Fig. 8, assuming a total dimming of 1% at a reference wavelength of 600 nm (Sing et al. 2011) for different starspot temperatures. Such corrections have been applied to the values of k reported in Fig. 7 for each of the four optical band, but the difference between the blue and the red bands remains substantial.

In order to investigate this variation, we have compared the observed transmission spectrum of WASP-36 b with sets of synthetic transmission spectra. These have been obtained by using two different codes, *petitCODE* and *VSTAR*. These two codes and the various models are described in the next two subsections.

5.1 *petitCODE*

For calculating synthetic transmission spectra we used *petitCODE* for self-consistent modelling of one-dimensional atmospheric structures and spectra (Mollière et al. 2015). *petitCODE* has recently been extended for deriving transmission spectra by directly calculating the transmission through planetary annuli as probed during transits. An effective planetary radius is then calculated from the combined transmission of all annuli. The transmission spectra include Rayleigh scattering of H_2 and He, using the cross-sections reported in Dalgarno & Williams (1962) and Chan & Dalgarno (1965), respectively. For verification purposes of our implementation of the transmission-spectrum calculations, we compared to the one-dimensional transmission spectra given in figs. 2 and 3 in Fortney et al. (2010), which yielded excellent agreement. We further added molecular cross-sections for TiO and VO, using an updated line list based on Plez (1998), available on the au-

thor’s website⁷ for TiO and a line list obtained from Bertrand Plez (private communication) for VO. The partition functions were obtained from Uffe Gråe Jørgensen’s website⁸ for TiO and Bertrand Plez (private communication) for VO, which is based on an updated partition function by Sauval & Tatum (1984); see also Gustafsson et al. (2008). As pressure broadening information was not available, we approximated the broadening coefficients using Equation (15) in Sharp & Burrows (2007). For this set of models we use an extended list of condensable species, comprising MgSiO_3 , Mg_2SiO_4 , SiC, Fe, Al_2O_3 , Na_2S , KCl, H_2O , TiO and VO. The chemical equilibrium abundances for the gas and condensed phase species in *petitCODE* are now calculated by a new chemical equilibrium code, which reliably works for temperatures between 60 – 20000 K and has been tested for consistency with the CEA code (Gordon & McBride 1994; McBride 1996). For the development of this code we made use of the methods and equations outlined in the CEA manual (McBride 1996).

Using the values reported in Table 4 for the parameters of WASP-36 b and its host star, we calculated self-consistent atmospheric structures. The stellar irradiation was calculated assuming a global average. As the flux is received by the planet with a cross-section of πR_b^2 , but is distributed over an area of $4\pi R_b^2$, this corresponds to a flux dilution factor of 1/4 when compared to the flux at the substellar point. We computed atmospheres for two different planetary metallicities: $[\text{Fe}/\text{H}]_b = -0.3$, which is close to the value reported for the host star (-0.26 ± 0.10 , Smith et al. 2012), and $[\text{Fe}/\text{H}]_b = 0.7$, which corresponds to the planet being ten times more enriched than its host star. For both metallicities we calculated two atmospheres: in the first case we did not consider the opacities of TiO and VO in the atmospheric structure calculation, whereas in the second case we did consider such opacity contributions. For the cases in which TiO and VO were not considered, we took the resulting two pressure-temperature structures and calculated three different transmission spectra to investigate the following three cases:

⁷ <http://www.pages-perso-bertrand-plez.univ-montp2.fr/>

⁸ http://www.astro.ku.dk/~uffegj/scan/scan_tio.pdf

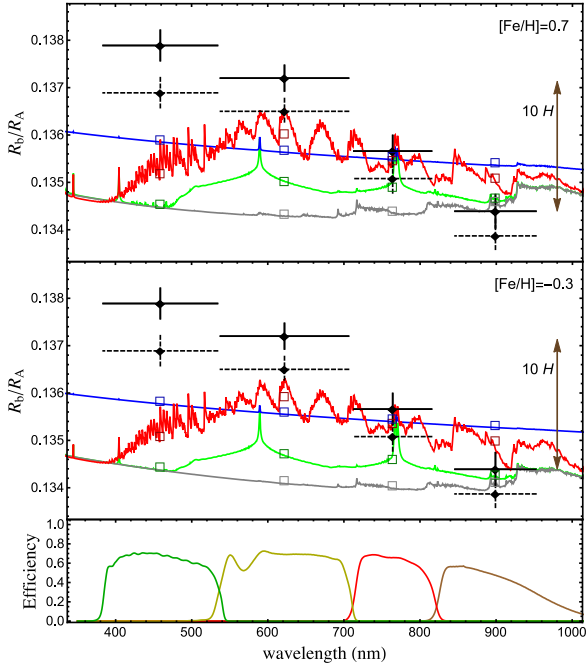


Figure 7. Variation of the ratio of the radii with wavelength. The black points are the weighted mean k values from the GROND observations. The vertical bars represent the relative uncertainties and the horizontal bars show the FWHM transmission of the passbands. The black points with dashed errorbars refer to the same measurements after correction for possible starspot activity. Synthetic spectra for WASP-36 b, obtained with the *petitCODE*, are shown as coloured lines. The green line is a standard prediction, the grey line shows the case in which Na and K are excluded, the blue line is as the grey one but with Rayleigh scattering increased by a factor of 1000, and the red line shows the case in which we consider the opacity contribution due to TiO and VO. Offsets are applied to the models to provide the best fit to our radius measurements. The atmospheres were computed for two different planetary metallicities: $[\text{Fe}/\text{H}]_b = -0.3$ (*top panel*) and $[\text{Fe}/\text{H}]_b = 0.7$ (*bottom panel*). Coloured boxes represent the predicted values for the three models integrated over the passbands of the observations. Transmission curves of the GROND filters are shown in the bottom panel. The size of ten atmospheric pressure scale heights ($10H$) is shown on the right of the plot.

- nominal case, using the same opacities as were used for obtaining the atmospheric structure;
- case without Na and K opacity;
- case without Na and K opacity and a H_2 Rayleigh cross-section enhanced by a factor 1000 in order to mimic strong Rayleigh-like scatterers.

In total we considered eight cases: 2×3 cases for the atmospheric structures calculated without TiO and VO, plus two cases for the atmospheric structures including TiO and VO. They are depicted in Fig. 7, and it is clear that none of the options explored above was able to reproduce the data, especially their steep slope.

The slope of the transit spectrum is given by (see, e.g., Lecavelier des Etangs et al. 2008)

$$\frac{dR_b}{d\log(\lambda)} = \alpha H \quad (1)$$

where α is the power law dependency of the opacity with respect to wavelength, $\alpha = d\log(\kappa)/d\log(\lambda)$, and H is the atmospheric scale height. The surface gravity of WASP-36 b is well constrained by its mass and radius measurements, and μ_m should have a value close to 2.3 amu if one assumes an atmosphere dominated by H_2 and He (de Wit & Seager 2013). For WASP-36 b the slope obtained for the synthetic transmission spectra is too small by a factor of ~ 4 when compared to the data. The minimum temperature in our atmospheric structure is ~ 1000 K. Rayleigh scattering ($\alpha = -4$) would thus require a very high atmospheric temperature, of at least 4000 K, in order to be consistent with the data.

5.2 VSTAR

We created a second set of models of the atmosphere of WASP-36 b with the Versatile Software for the Transfer of Atmospheric Radiation (VSTAR; Bailey & Kedziora-Chudczer 2012). VSTAR is a robust line-by-line radiative transfer solver, which has been successfully applied to the atmospheres of cool stars, solar system planets, and hot Jupiters (Zhou et al. 2015). For WASP 36 b, the Rayleigh and Mie scattering capabilities were used for attempting to model the dramatic increase with radius at bluer wavelengths. Rayleigh scattering from a H-He atmosphere alone is not able to describe the change in radius for WASP 36 b that we have measured. A Mie scattering haze of small particles can be introduced to compensate for a large portion of the short wavelength absorption.

Such a scattering haze is introduced within the radiative transfer model and is dependent upon the optical depth per horizontal layer, the refractive indices of the scattering material across relevant wavelengths, and the radii of the particles themselves. Scattering atmospheric particles with radii ranging from 0.01 to $0.1 \mu\text{m}$ were tested. The distribution in sizes for a given median radius is described by a power law distribution with an effective variance of $0.01 \mu\text{m}$ (Mishchenko et al. 2002). Approximately half the slope can be derived with particle sizes around $0.03 - 0.04 \mu\text{m}$. Changing the distribution of these particles vertically throughout the atmosphere can shape the Mie scattering contribution. In systems with sufficient data, this can be fit to provide information about the cloud and haze distribution on the planet. The opaqueness of the layers set by the optical depth per height effects the spectrum particularly for upper layers where the transmission path length is longer. Too great an optical depth at a given layer will create a flattened spectrum towards longer wavelengths masking molecular features. Because of the shift in the relative radius from blue to red wavelengths for WASP 36 b it is unlikely that a very opaque cloud is present high in the atmosphere.

In Fig. 9 transmission spectral curves without molecular features are shown. The variation in the radius is due solely to scattering by molecular species or clouds and hazes. The various lines correspond to different values of the optical depth in the upper atmosphere over 1000 km. The model with H-He Rayleigh scattering alone (dashed cyan line) does not compensate for the steep rise in absorption towards blue wavelengths. The optical depth distributions shown are illustrative of the effects of clouds and hazes. Blue scattering

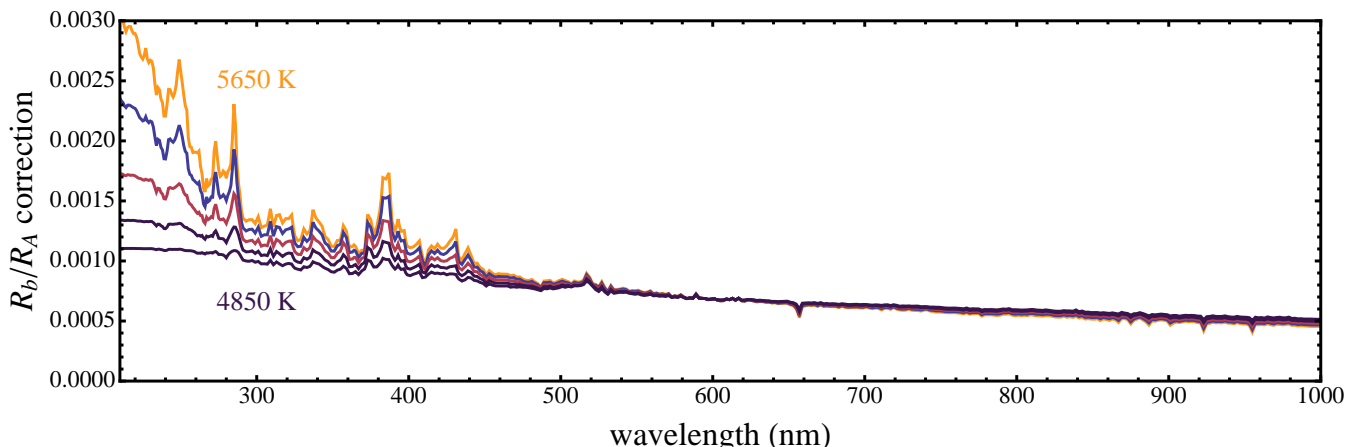


Figure 8. The effect of unocculted starspots on the transmission spectrum of WASP-36 b, considering a 1% flux drop at 600 nm. We adopted a stellar temperature of $T_{\text{eff}} = 5960$ K, while the starspot coverage was modelled using a grid of stellar atmospheric models of different temperature ranging from 5650 K (yellow line) to 4850 K (purple line), in steps of 250 K.

haze in a highly extended atmosphere could possibly produce the large scale height distribution of radii.

Layer-by-layer calculations for varying optical depth were trialled, but we found that they cannot compensate for the unusually steep absorption. The scattering properties were based upon those of enstatite, which is a species likely responsible for the blue light scattering in the hot Jupiter HD 189733 b (Zahnle et al. 2009). Other species with weaker attenuation at blue wavelengths, such as some sulphurous molecular species, may better compensate for the blue light absorption in the planet’s transit. It is possible that along with strong Mie and Rayleigh scattering – perhaps from an extended scattering haze – that absorption in blue light from a molecular species is also present.

Relatively few species absorb in blue visible light wavelengths. Zahnle et al. (2009) showed that sulphanyl (HS) has an absorption spectrum which is effective at short wavelengths, and they derived the absorption cross section for the species at some UV and blue wavelengths. Unfortunately no information on the species for longer wavelengths is currently available and we could not calculate the corresponding radiative transfer in the atmosphere of WASP-36 b using the absorption cross section with VSTAR.

6 CONCLUSIONS

We have presented new broad-band photometric observations of five transit events in the WASP-36 planetary system, which is composed of a relatively young G2 V star and a massive hot Jupiter. Four transits were observed with the GROND instrument, which supports observations in four optical bands simultaneously; another single-band transit observation was obtained with the CAHA 1.23 m telescope. We fitted the light curves using the JKTEBOP code, and revised the orbital ephemeris and physical parameters of the system. Our results are consistent with and more precise than previous measurements.

We searched for a variation of the measured radius of WASP-36 b as a function of wavelength, by determining the ratio of the planet’s radius to that of the star in the four

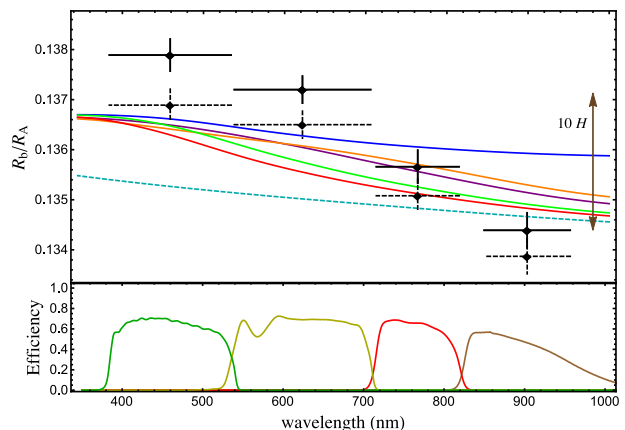


Figure 9. Variation of the ratio of the radii with wavelength, same as in Fig. 7. Synthetic spectra for WASP-36 b, obtained with the VSTAR code (see Sect. 5.2), are shown as coloured lines. The different lines correspond to varying optical depth with height, indicative of the Mie scattering particle distribution. Pure Rayleigh scattering without the effects of clouds is shown with the dashed cyan curve. No molecular absorption is included in these models.

GROND passbands. Our data clearly show an increase of the planetary radius in the bluer bands. The variation between g' and z' is more than $10 H$ with a significance level larger than 5σ .

We compared the multi-band measurements with the predictions of several theoretical models of planetary atmospheres. Synthetic spectra were computed using *petitCODE* for self-consistent atmospheric structures and two opposite planetary metallicities; various cases with strong absorbers (TiO and VO), without Na and K opacity and with strong Rayleigh-like scattering process were investigated. Furthermore, the VSTAR code was also utilised to produce atmospheric models in which the planetary-radius variation is only due to scattering by molecular species or clouds and hazes. Different models were presented varying the optical depth of the atmosphere. However, in no case was our mod-

els were able to reproduce the observed spectrum. Neither the presence of gaseous oxides nor strong Rayleigh scattering seems to be the cause of the steep slope in the transmission observations. The existence of an absorber which reproduces the observed transmission photometry due to its line opacities is therefore more likely, but the exact nature and origin of such an absorber is speculative.

In conclusion, the mechanism responsible for the steep slope in the transmission spectrum of WASP-36 b remains difficult to constrain. Further observations of WASP-36 b transits are suggested, especially with a photometer in the *U* band or with a spectrograph able to cover a large spectral range at optical wavelengths.

ACKNOWLEDGEMENTS

This paper is based on observations collected with the MPG 2.2 m telescope located at the ESO Observatory in La Silla, Chile, and with the Zeiss 1.23 m telescope at the Centro Astronómico Hispano Alemán (CAHA) at Calar Alto, Spain. Operation of the MPG 2.2 m telescope is jointly performed by the Max Planck Gesellschaft and the European Southern Observatory. Operations at the Calar Alto telescopes are jointly performed by the Max Planck Institute for Astronomy (MPIA) and the Instituto de Astrofísica de Andalucía (CSIC). GROND was built by the high-energy group of MPE in collaboration with the LSW Tautenburg and ESO, and is operated as a PI-instrument at the MPG 2.2 m telescope. LM thanks Yan Betremieux for useful discussion. The reduced light curves presented in this work will be made available at the CDS (<http://cdsweb.u-strasbg.fr/>). We thank the anonymous referee for their useful criticisms and suggestions that helped us to improve the quality of this paper. The following internet-based resources were used in research for this paper: the ESO Digitized Sky Survey; the NASA Astrophysics Data System; the SIMBAD data base operated at CDS, Strasbourg, France; and the arXiv scientific paper preprint service operated by Cornell University.

REFERENCES

- Bailey J., Kedziora-Chudczer L., 2012, *MNRAS*, 419, 1913
 Bean J. L., Miller-Ricci Kempton E., Homeier D., 2010, *Nature*, 468, 669
 Bean J. L., et al., 2011, *ApJ*, 743, 92
 Bott K., Cotton D., Bailey J., Kedziora-Chudczer L., 2016, in prep.
 Carter J. A., Winn J. N., 2009, *ApJ*, 704, 51
 Chan, Y. M., Dalgarno, A. 1965, *Proc. Phys. Soc.*, 85, 227
 Chen G., et al., 2014, *A&A*, 563, A40
 Ciceri S., et al., 2015, *A&A*, 577, A54
 Claret A., 2004, *A&A*, 424, 919
 Dalgarno, A. Williams, D. A. 1962, *ApJ*, 136, 690
 Demarque P., Woo J.-H., Kim Y.-C., Yi S. K., 2004, *ApJS*, 155, 667
 de Wit J., Seager S., 2013, *Science*, 342, 1473
 Désert J.-M., Vidal-Madjar A., Lecavelier Des Etangs A., Sing D., Ehrenreich D., Hébrard G., Ferlet R., 2008, *A&A*, 492, 585
 Dotter A., et al., 2008, *ApJS*, 178, 89
 Fischer, P. D., et al., 2016, *ApJ*, submitted, arXiv:1601.04761
 Fortney J. J., Marley M. S., Hubickyj O., Bodenheimer P., Lissauer J. J., *AN*, 326, 925
 Fortney J. J., Lodders K., Marley M. S., Freedman R. S., 2008, *ApJ*, 678, 1419
 Fortney J. J., Shabram M., Showman A. P., 2010, *ApJ*, 709, 1396
 Gibson N. P., Aigrain S., Barstow J. K., Evans T. M., Fletcher L. N., Irwin P. G. J., 2013a, *MNRAS*, 428, 3680
 Gibson N. P., Aigrain S., Barstow J. K., Evans T. M., Fletcher L. N., Irwin P. G. J., 2013b, *MNRAS*, 436, 2974
 Gordon S., & McBride B. J., 1994, *Computer Program for Calculation of Complex Chemical Equilibrium Compositions and Applications (NASA)*
 Greiner J., et al., 2008, *PASP*, 120, 405
 Gustafsson B., Edvardsson B., Eriksson K., 2008, *A&A*, 486, 951
 Huitson C. M., et al., 2013, *MNRAS*, 434, 3252
 Jordà A., et al., 2013, *ApJ*, 778, 184
 Knutson H. A., Howard A. W., Isaacson H., 2010, *ApJ*, 720, 1569
 Lecavelier des Etangs, A., Pont, F., Vidal-Madjar, A., Sing, D., 2008, *A&A*, 481, L83
 Maciejewski G., et al., 2016, *Acta Astronomica* in press, arXiv:1603.03268
 Mallonn M., et al., 2015, *A&A*, 580, A60
 Mancini L., et al., 2014a, *A&A*, 562, A126
 Mancini L., et al., 2014b, *A&A*, 568, A127
 Mancini L., et al., 2014c, *MNRAS*, 443, 2391
 Mancini L., et al., 2015, *A&A*, 579, A136
 Mancini L., & Southworth J., 2016, in *Twenty years of giant exoplanets*, Proceedings of the Haute Provence Observatory Colloquium, Ed. I. Boisse, O. Demangeon, F. Bouchy, L. Arnold, p. 120
 McBride B. J., 1996, *Computer Program for Calculation of Complex Chemical Equilibrium Compositions and Applications II (NASA)*
 Mishchenko M. I., Travis L. D., Lacis A. A., 2002, “Scattering, absorption, and emission of light by small particles”, Cambridge University Press
 Mollière P., van Boekel R., Dullemond C., Henning T., Mordasini C., *ApJ*, 813, 47
 Murgas F., Pallè E., Zapatero Osorio M. R., Nortmann L., Hoyer S., Cabrera-Lavers A., 2014, *A&A*, 563, A41
 Nascimbeni V., Piotto G., Pagano I., Scandariato G., Sani E., Fumana M., 2013, *A&A*, 559, A32
 Nikolov N., et al., 2013, *A&A*, 553, A26
 Nikolov N., et al., 2014, *MNRAS*, 437, 46
 Nikolov N., et al., 2015, *MNRAS*, 447, 463
 Parviainen H., Pallè E., Nortmann L., Nowak G., Iro N., Murgas F., Aigrain S., 2016, *A&A*, 585, A114
 Pierini D. et al., 2012, *A&A*, 540, A45
 Pietrinferni A., Cassisi S., Salaris M., & Castelli F., 2004, *ApJ*, 612, 168
 Plez B., 1998, *A&A*, 337, 495
 Pont, F., Sing, D. K., Gibson, N. P., Aigrain, S., Henry G., Husnoo N., 2013, *MNRAS*, 432, 2917
 Sauval A. J., Tatum J. B. 1984, *ApJS*, 56, 193
 Sedaghati E., Boffin H. M. J., Csizmadia S., Gibson N., Kabath P., Mallonn M., Van den Ancker M. E., 2015, *A&A*, 576, L11
 Sharp C. M., & Burrows A., 2007, *ApJS*, 168, 140
 Sing D. K. et al., 2011, *MNRAS*, 416, 1443
 Sing D. K. et al., 2013, *MNRAS*, 436, 2956
 Sing D. K. et al., 2015, *MNRAS*, 446, 2428
 Sing D. K. et al., 2016, *Nature*, 529, 59
 Smith A. M. S., et al., 2012, *AJ*, 143, 81
 Southworth J., 2012, *MNRAS*, 426, 1291
 Southworth J., 2013, *A&A*, 557, 119
 Southworth J., et al., 2012, *MNRAS*, 422, 3099
 Southworth J., et al., 2014, *MNRAS*, 444, 776
 Southworth J., et al., 2015, *MNRAS*, 447, 771
 Stevenson K. B., Bean J. L., Seifahrt A., Désert J.-M., Madhusud-

- han N., Bergmann M., Kreidberg L., Homeier D., 2014, *AJ*, 147, 161
- Stevenson K. B., Bean J. L., Seifahrt A., Gilbert G. J., Line, M. R., Desert J.-M., Fortney J. J., 2016, *ApJ*, 817, 141
- VandenBerg D. A., Bergbusch P. A., & Dowler P. D., 2006, *ApJS*, 162, 375
- Winn J. N. 2010, in *Exoplanets*, ed. S. Seager (The University of Arizona Press), 56
- Zahnle K. J., et al., 2009, *ApJ*, 701, L20
- Zhou G., Kedziora-Chudczer L., Bayliss D. D. R., Bailey J., 2013, *ApJ*, 774, 118
- Zhou G., et al., 2015, *MNRAS*, 454, 3002

This paper has been typeset from a $\text{\TeX}/\text{\LaTeX}$ file prepared by the author.